Chemical Engineering Journal 405 (2021) 126661

Contents lists available at ScienceDirect

Chemical Engineering Journal

journal homepage: www.elsevier.com/locate/cej

Bisphenol S-doped g-C_3N_4 nanosheets modified by boron nitride quantum dots as efficient visible-light-driven photocatalysts for degradation of sulfamethazine

Qiuting Zhang[a,1], Yanrong Peng[a,1,*], Yan Lin[a,b], Shaohua Wu[a,b], Xiaochao Yu[a,b], Chunping Yang[a,b,c,*]

[a] College of Environmental Science and Engineering, Hunan University and Key Laboratory of Environmental Biology and Pollution Control (Hunan University), Ministry of Education, Changsha, Hunan 410082, China
[b] Guangdong Provincial Key Laboratory of Petrochemical Pollution Processes and Control, School of Environmental Science and Engineering, Guangdong University of Petrochemical Technology, Maoming, Guangdong 525000, China
[c] Hunan Province Environmental Protection Engineering Center for Organic Pollution Control of Urban Water and Wastewater, Changsha, Hunan 410001, China

HIGHLIGHTS

- The novel metal-free BNQDs/BPS-CN photocatalysts are successfully synthesized.
- The photocatalysts show superior photocatalytic activities and stability in photodegradation of sulfamethazine.
- Enhanced visible light absorption and charge transfer from BNQDs/BPS-CN are recorded.
- A pathway for photocatalytic degradation of sulfamethazine is proposed.

ARTICLE INFO

Keywords:
Graphitic carbon nitride
Boron nitride quantum dots
Bisphenol S
Photocatalysis
Sulfamethazine

ABSTRACT

Antibiotics may pose a great risk to ecosystem and human health. Photocatalysis, as a low-cost and environmentally friendly technology is widely used for the removal of antibiotics from wastewater. Graphitic carbon nitride (g-C_3N_4) has shown promising prospects in visible light photocatalysis, while its photocatalytic performance is greatly limited because of the sluggish charge separation and transfer. In this work, metal-free boron nitride quantum dots (BNQDs) modified bisphenol S (BPS)-doped g-C_3N_4 nanosheets (BNQDs/BPS-CN) heterojunction was synthesized to overcome these defects and applied in photodegradation of sulfamethazine (SMZ, a typical antibiotic) under the visible light. Multifarious characterization methods were used to explore the structure, porosity, elemental composition, optical performances, photo-electrochemical properties and photocatalytic performances of as-prepared BNQDs/BPS-CN composites. The degradation efficiency of SMZ with BNQDs/BPS-CN-4 composite reaches 100% within 60 min, and the rate constant is 13.7 times higher than that of pure g-C_3N_4. This phenomenon is because of the shrinking band gap width and the introduction of electronegative BNQDs, which is conducive to the absorption of visible light and high-efficiency separation of photoexcited charge carriers. Meanwhile, the results of free radical trapping experiments and electron spin resonance characterization prove that the photogenerated holes and superoxide radicals play predominant roles in the photodegradation of SMZ. This study proposes an effective mechanism for the construction of novel visible-light-driven photocatalysts using metal-free two-dimensional materials and quantum dots, which can be applied in the treatment of organic contaminants.

1. Introduction

Antibiotics are widely used in disease prevention and treatment of bacterial infection [1]. However, some antibiotics are discharged into the environment due to the incomplete metabolism of the organism, causing adverse influence and a serious threat to the ecosystem and

* Corresponding authors at: College of Environmental Science and Engineering, Hunan University, Changsha, Hunan 410082, China.
E-mail addresses: pengyr@hnu.edu.cn (Y. Peng), yangc@hnu.edu.cn (C. Yang).
[1] These authors contribute equally to this paper.

https://doi.org/10.1016/j.cej.2020.126661
Received 24 June 2020; Received in revised form 9 August 2020; Accepted 11 August 2020
Available online 14 August 2020
1385-8947/

human health [2,3]. Among the different kinds of antibiotics, sulfonamides (SAs) have been widely used in animal husbandry, aquaculture, and medicine. However, SAs possess stable physicochemical properties [4], once discharged into the environment they can be readily accumulated in the surroundings. Besides, even if SAs exist in the environment with a relatively low concentration (mg/L to μg/L) [5], the wide-ranging residues in the surface water, underground water and the effluent of wastewater treatment plants, still may cause public security problem because of their high toxicity. Conventional wastewater treatment methods, such as biological treatment [2,6], adsorption techniques [7], and chemical reactions [8], suffer from the disadvantages of low removal efficiency, high cost, complex operational process, and serious secondary pollution [9]. Therefore, it is significant to exploit a simple, inexpensive, and high-efficiency approach to remove sulfonamides from wastewater. In recent years, advanced oxidation technologies [10,11] including electrochemical treatment [12], and photocatalysis technology [13,14], have been successfully applied to the treatment for organic pollutants in the wastewater. Among them, semiconductor photocatalytic technology is considered as a promising treatment method because of the mild reaction condition and utilization of sunlight [15,16].

Graphitic carbon nitride (g-C_3N_4), as a typical metal-free polymer semiconductor, has received tremendous attention due to its outstanding thermal, optical properties, and physicochemical stability [17–20]. Moreover, the suitable optical band gap (2.7 eV) makes g-C_3N_4 an excellent visible light response and can be applied for photocatalytic degradation of organic pollutants [18,21,22]. However, some defects including low surface area, sluggish charge dissociation, and fast recombination of photogenerated charge carriers restrict the photocatalytic performance of g-C_3N_4 [23,24]. Therefore, to facilitate the separation of photogenerated electron-hole pairs and thus enhance the photocatalytic performance of g-C_3N_4, various methods have been adopted to modify it. Stripping bulk g-C_3N_4 into ultrathin porous nanosheets and constructing layered nanostructures are promising methods to enlarge the specific surface area and shorten the transfer route of charge, which give rise to the increasement of active reaction sites and charge separation efficiency [25–27]. For instance, Yang et al. [17] fabricated the g-C_3N_4 with ultrathin and porous nanostructures by a precursor-surface-etching method, which significantly improved the photocatalytic degradation activity of oxytetracycline hydrochloride.

Element doping is another modified approach to adjust the electronic structure and band gap of g-C_3N_4, which improves the utilization efficiency of visible light and promotes the charge separation. Many studies have shown that element doping, such as O, N, P, and S can effectively straiten the band gap of g-C_3N_4 and further enhance its photocatalytic activity [28–30]. Similar to elemental doping, the doping of organic compounds containing aromatic structures can also improve the photocatalytic activity of g-C_3N_4. For instance, naphthalene-modified g-C_3N_4 (GCN) composite was successfully prepared via thermal polymerization of urea with naphthoic acid and showed better photocatalytic hydrogen evolution performance than that of original g-C_3N_4 [31]. Karjule et al. fabricated the CN polymers with PAHs sites, and the CN-PAH polymers exhibited high photocatalytic activity for the hydrogen evolution reaction. The improvement of photocatalytic performance was attributed to the fact that the conjugation effect of the new PAHs groups favored visible light absorption and inhibited the recombination of photogenerated electron-hole pairs [32]. Therefore, we inferred that incorporating bisphenol S (BPS) containing diphenyl ring structure into the g-C_3N_4 framework might improve its photocatalytic activity by narrowing the band gap to promote the visible light absorption capacity and facilitating the separation of photogenerated electron-hole pairs.

Besides, the construction of heterojunction is an available method to enhance the photocatalytic performance of semiconductor photocatalysts because it can efficiently promote charge transportation and restrain the recombination of photogenerated electron-hole pairs [33–35]. Hexagonal boron nitride (h-BN), as an attractive two-dimensional semiconductor with a similar structure to graphene, has gained wide attention because of the unique physicochemical properties, such as excellent photoelectric properties, high thermal conductivity, exceptional chemical stability, and high specific surface area [36–38]. Recent studies have proved that h-BN as co-catalyst could effectively promote the photocatalytic activity of photocatalysts, which makes it highly attractive for application in the field of photocatalysis [39,40]. Moreover, when the size of semiconductor particle is decreased to the quantum dots level, the semiconductor quantum dots as co-catalyst can effectively promote the separation of photogenerated charge carriers and thus enhance the photocatalytic performance of photocatalysts because of the edge effects and defect centers [41,42]. Boron nitride quantum dots (BNQDs), a spherical particle at 1–10 nm in diameter, exhibited strong electrostatic attraction to photoinduced holes due to the presence of negatively charged oxygen-containing groups, which beneficial for the separation of photogenerated electron-hole pairs [17,43–45]. BNQDs as the co-catalyst could efficiently improve the visible-light photocatalytic activity of ultrathin porous g-C_3N_4. Therefore, we envisioned that combine BNQDs with modified g-C_3N_4 base photocatalyst toward structure a heterostructured photocatalytic system for the photocatalysic degradation of organic pollutants.

Herein, we designed and fabricated the BNQDs modified BPS-doped g-C_3N_4 nanosheet (BNQDs/BPS-CN) heterojunction photocatalysts. The behavior of photogenerated charge carriers is investigated by steady-state fluorescence analysis and photoelectrochemical technique. The photocatalytic degradation performance of sulfamethazine (SMZ) by BNQDs/BPS-CN is evaluated. Furthermore, the possible photocatalytic mechanism of BNQDs/BPS-CN under visible light irradiation is deeply investigated.

2. Experimental section

2.1. Materials

Bisphenol S (BPS, 99.5%) was obtained from Guangzhou Hongcheng Biological Technology Co, Ltd (Guangzhou, China). Urea, boric acid, melamine and ethanol were bought from Sinopharm Chemical Reagent Co. Ltd. All reagents were of analytical purity and used directly without further disposal. De-ionized water (18.25 MΩ·cm^{-1}) obtained from the Millipore Mill-Q purification instrument was employed throughout all the experiments.

2.2. Preparation of photocatalysts

2.2.1. Preparation of BPS-CN nanosheets

BPS-CN nanosheets was prepared by a simple calcination method [46]. Briefly, 10 g of urea and 15 mg of BPS were mixed thoroughly in a mortar. Then the obtained mixture was loaded into 50 mL ceramic crucible with a cover. The crucible was tightly wrapped with tin foil before heated to 550 °C for 3 h with a heating rate of 3 °C min^{-1} in the muffle furnace and then cooled down naturally. The resulted light brown powder was denoted as BPS-CN precursor. Subsequently, the precursor was loaded into a rectangle crucible without cover and heated to 450 °C for 3 h under a heating rate of 8 °C min^{-1}. The final as-synthesized brown sample was the BPS-CN. Besides, pure g-C_3N_4 was prepared with the same process as BPS-CN without adding BPS.

2.2.2. Preparation of BNQDs

The BNQDs was prepared by a typical hydrothermal process [47]. Specifically, 0.150 g of boric acid and 0.035 g of melamine were mixed and dissolved in 30 mL deionized water and stirring for 20 min. Next, the obtained solution was placed into a Teflon-lined autoclave and subsequently heated at 200 °C for 20 h. After the hydrothermal reaction and cooling down to the room temperature, the solution was filtered with a 0.22 μm organic phase ultrafiltration membrane. Then, the filter

liquor was dried in a freeze dryer, and the collected sample was denoted as BNQDs.

2.2.3. Preparation of BNQDs/BPS-CN

The preparation of BNQDs/BPS-CN photocatalysts was as follows: 0.300 g of BPS-CN was added into 60 mL ethanol followed by ultrasonic agitation evenly for 30 min. Next, a suitable amount of BNQDs alcohol solution (1 mg L^{-1}) was dropped into the suspension followed by sonication for 1 h. Subsequently, the mixture solution was stirred at 60 °C until the ethanol was evaporated completely. The final powder was labeled as BNQDs/BPS-CN-X, where X (2, 3, 4, 5, 6 mL) represented the added volume of the BNQDs alcohol solution.

2.3. Characterization

The section of characterization is shown in the supporting information.

2.4. Photocatalytic experiments

The photocatalytic activities of the as-prepared samples were evaluated by the SMZ degradation at room temperature under visible light irradiation. The 300 W Xe lamp with a 420 nm cut-off filter was employed as the visible light source. In all photodegradation experiments, 25 mg photocatalyst was added into a quartz reactor containing SMZ aqueous solution (100 mL, 20 mg/L). The mixture was stirred adequately in the dark for 30 min to achieve the adsorption–desorption balance between the photocatalyst and SMZ. Next, the suspension was placed under the lamp source. At a certain time interval, 2 mL of suspension was centrifuged and filtered through a 0.22 μm organic phase filter to separate suspended solids. The concentration of filtrate was determined by HPLC (Agilent, Waldbronn, Germany), which furnished a UV–vis detector. Kromasil C18 column (5 μm, 4.6 mm × 250 mm) was as the column at 30 °C. The mobile phase of SMZ was acetonitrile and 0.1% (v/v) of acetic acid aqueous solution (45:55, A/B), and the flow rate was 1 mL min^{-1}, the detector was at a wavelength of 270 nm.

Besides, the intermediate products of SMZ in the photocatalytic degradation process were determined by UPLC-MS/MS technology. The detail information is described in the supporting Information.

2.5. Photoelectrochemical experiments

The photoelectrochemcial studies were conducted on a CHI 760E electrochemical workstation with a three-electrode cell. The platinum electrode and the saturated calomel electrode (SCE) were used as the counter electrode and the reference electrode, respectively. The construction process of the working electrode was made as follows: 5 mg photocatalyst was dispersed in 1.0 mL mixture solution (ethanol and 0.05% Nafion), then 0.1 mL suspension was dropped onto the clean and dry FTO electrode (1.0 cm × 2.0 cm). The transient photocurrent tests, Mott-Schottky plots, and the electrochemical impedance spectroscopy of the prepared samples were performed in 0.5 M Na_2SO_4 solution.

3. Results and discussion

3.1. Characterization of photocatalysts

The synthetic pathways of g-C_3N_4 and BPS-CN are displayed in Scheme S1. During the melamine formation step, BPS was doped into the main chain of g-C_3N_4 by copolymerization. Doped S atoms and diphenyl ring structures have appeared in the triazine based structure [48].

The microstructures of as-prepared samples were detected by transmission electron microscope (TEM) and high-resolution transmission electron microscopy (HRTEM). As displayed in Fig. 1a and b, both BPS-CN and BNQDs/BPS-CN present a stacked sheet-like structure with some folds, which are similar to the structure of g-C_3N_4 (Fig. S1a). In addition, there are many pores in BPS-CN nanosheets. To prove the existence of quantum dots, the HRTEM images of BNQDs and BNQDs/BPS-CN were provided. From Fig. S1b, it can be obviously seen that the BNQDs present a spherical structure with a profile diameter of about 3 nm, which compliances with the previous reports [43,47]. As for BNQDs/BPS-CN (Fig. 1c), BNQDs are evenly distributed on the surface of BPS-CN nanosheets, which demonstrates that BNQDs have been successfully introduced onto the surface of BPS-CN. Meanwhile, as displayed in the insert image of Fig. 1c, BNQDs have a distinct lattice spacing about 0.21 nm, corresponding to the (1 0 0) hexagonal pattern for BN [49]. Additionally, EDX analysis of BNQDs/BPS-CN composite was performed. As shown in Fig. S2, the as-prepared BNQDs/BPS-CN-4 composite is consisted of elemental C, N, O, S, B, and the weight percentages are about 60.58%, 33.50%, 3.46%, 0.98%, 1.48%, respectively. The HAADF-STEM element mapping of BNQDs/BPS-CN (Fig. 1d) shows the elements (B, C, N, O and S) are all evenly distributed on the BNQDs/BPS-CN nanosheets, which further confirms that BPS is successfully doped into the g-C_3N_4 framework and BNQDs are well dispersed on BPS-CN nanosheets.

The crystalline structures of the as-synthesized materials were investigated by XRD. As displayed in Fig. 2a, g-C_3N_4 has two main diffraction peaks at $2\theta = 12.9^\circ$ and 27.8°, which can be corresponded to the (1 0 0) and (0 0 2) crystal planes of g-C_3N_4 (JCPDS No. 87–1526), respectively, associating with the overlap of nonplanar units and the periodic stacking of layers in the conjugated aromatic system [18,50]. These results prove the successful synthesis of g-C_3N_4. After doping with BPS, the (0 0 2) peak at 27.8° of g-C_3N_4 shift to 27.1° in BPS-CN due to the increase of stacking distance [46]. Besides, the characteristic peaks of boron nitride can't be detected in the BNQDS/BPS-CN composite, this may because of the relatively low content of boron nitride [17]. In addition, solid-state ^{13}C NMR technique was employed to confirm the introduction of the BPS. As shown in Fig. S3, two characteristic peaks of heptazine rings at 157.0 ppm and 164 ppm correspond to C-N_3 and external-NH_2 groups (N_2C-NH_2 unit), respectively [32]. New peaks at 125.6 and 127.2 ppm are attributed to the incorporated aromatic carbon in BPS-CN [51]. The result evidences the existence of benzene ring structure in g-C_3N_4 nanosheets.

The X-ray photoelectron spectroscopy (XPS) was performed to reveal the elemental composition and chemical status of the as-prepared catalysts. As shown in Fig. 2b, all samples contain C, N, and O elements, while BNQDs/BPS-CN also contains B element resulting from the doped BNQDs. Besides, there is no obvious characteristic peak of S in the XPS spectra of BPS-CN and BNQDs/BPS-CN, which may be due to the low doping concentration of BPS [48]. Furthermore, the high-resolution XPS spectrums of C 1s, N 1s, B 1s, and S 2p were measured. As displayed in Fig. 2c, the main peak of C 1s in all samples is centered at 287.9 eV, which can be ascribed to the N−C═N sp^2-hybridized carbon atom [52]. When doped with BPS, the other C 1s peak at 285.6 eV is shifted to 285.2 eV with a slightly increased intensity, which is due to the graphite sp^2 carbon (C−C) deriving from the incorporated BPS [53]. Fig. 2d displays N 1s spectrums in the as-prepared samples. The N 1s peaks in g-C_3N_4 are divided into three peaks. The strongest typical peak at 398.7 eV corresponds to the hybridized sp^2 aromatic N (C−N═C), the peaks located at 400.03 eV and 401.1 eV are assigned to the N-$(C)_3$ groups of bridging nitrogen atoms and amino functional group (C-N-H), respectively [19]. BPS-CN shows similar N 1s XPS spectra to that of g-C_3N_4, but the bridging tertiary nitrogen (400.03 eV) peak intensity of BPS-CN is relatively weaker than that of g-C_3N_4. It may be because that BPS doping changes the periodicity of g-C_3N_4 [46]. Compared with BPS-CN, the N 1s peaks at 398.42 eV and 399.92 eV in BNQDs/BPS-CN are ascribed to the N–B and C–N–B bond, respectively [54]. Furthermore, the high-resolution spectrum of S 2p is displayed in Fig. 2e, the S 2p spectrum can be deconvoluted into two major components and each component can be divided into two peaks. The peaks at 163.4 and 164.5 eV can be assigned to $2p_{3/2}$ and $2p_{1/2}$ of C-S-C bonds [55,56].

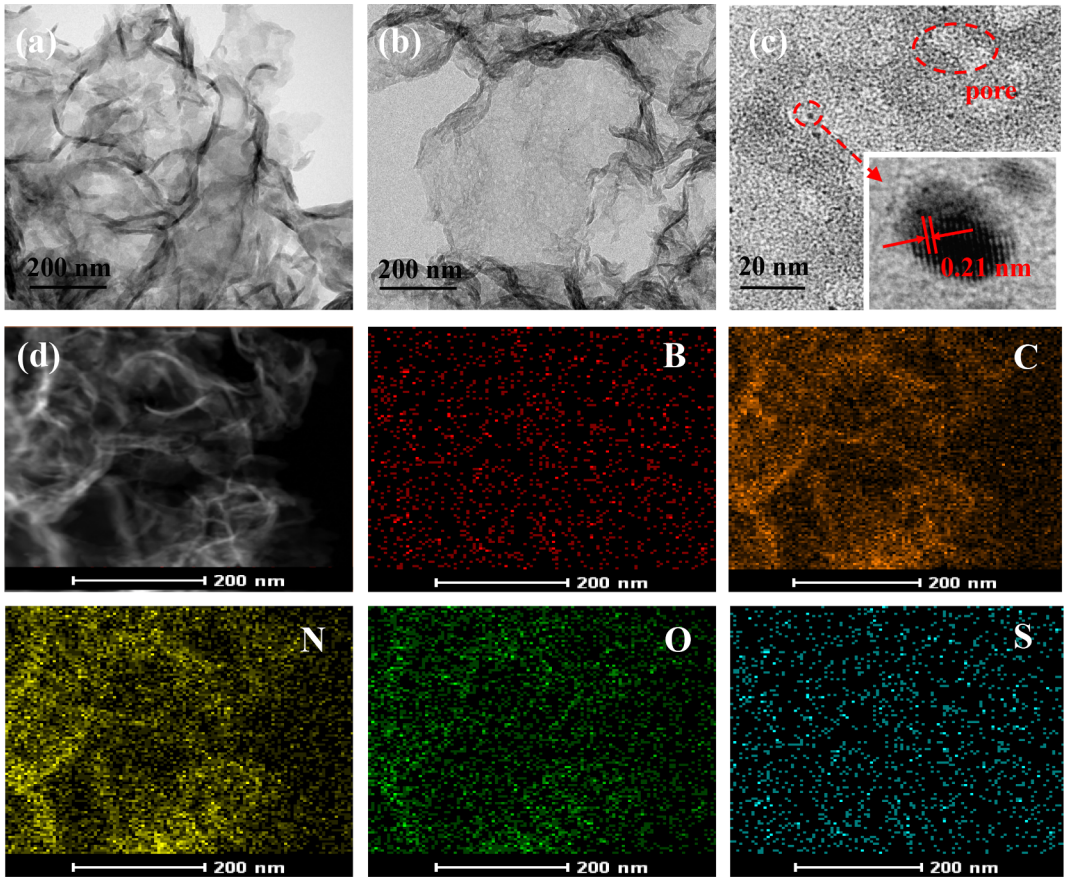

Fig. 1. TEM images of (a) BPS-CN, (b) BNQDs/BPS-CN; (c) HRTEM image of BNQDs/BPS-CN; (d) HAADF-STEM image and EDS mapping images of BNQDs/BPS-CN.

Meanwhile, the peaks corresponding to $2p_{3/2}$ and $2p_{1/2}$ of S-O from the doping of BPS are positioned at 167.3 and 168.2 eV, respectively [57,58]. Besides, in the B 1 s spectrum of BNQDs/BPS-CN (Fig. 2f), the peak located at 190.69 eV corresponds to the B–N bond and the other peak at 191.48 eV is related to the B—O bond. According to the above results, it can be concluded that BPS have been successfully doped into the framework of g-C_3N_4 and BNQDs have been introduced onto the surface of BPS-CN nanosheets.

To further investigate the morphology of the obtained catalysts, the porosity and BET surface area (S_{BET}) were estimated by nitrogen adsorption–desorption isotherms. The results are displayed in Fig. 3 and Table S1. As shown in Fig. 3, all samples reveal typical type IV isotherms, indicating that these samples possess mesoporous structures. In addition, BNQDs/BPS-CN has the largest BET surface area about 172.69 $m^2\ g^{-1}$ (Table S1). Generally, a larger S_{BET} can endow more reaction sites for photocatalysts. Therefore, BNQDs/BPS-CN has the highest photocatalytic activity among the three samples.

UV–vis DRS was used to identify the optical properties of the samples. As shown in Fig. 4a, the light-absorption edge of pure g-C_3N_4 nanosheets is located at 470 nm. After doping with BPS, the absorption edge of BPS-CN exhibits an apparent redshift compared with pure g-C_3N_4 nanosheets, which demonstrates that BPS doping into the g-C_3N framework can greatly broaden the spectral response range. Furthermore, the absorption edge of BNQDs/BPS-CN obtained by modifying of BPS-CN with BNQDs is similar to that of BPS-CN, while the absorption intensity of the sample is slightly increased. The bandgap edge of g-C_3N_4 and BPS-CN can be determined by the Kubelka-Munk equation (Supporting information). As presented in Fig. 4b, the Eg of g-C_3N_4 and BPS-CN are calculated to be 2.72 eV and 2.23 eV, respectively. The results validate that the doping of BPS can obviously straiten the band gap of g-C_3N_4. The valence band potential (E_{VB}) of g-C_3N_4 and BPS-CN are further analyzed through VB XPS spectra. From Fig. S4, it can be seen that the position of the VB edge of BPS-CN is located at about 1.61 eV, which is similar to that of g-C_3N_4 (1.65 eV). These results demonstrate that BPS doping doesn't influence the position of VB edge of g-C_3N_4. The position of the conduction band (CB) edge of g-C_3N_4 and BPS-CN can be calculated using the following equation:

$$E_{CB} = E_{VB} - -E_g$$

The calculated CB potentials are −0.98 eV and −0.62 eV for g-C_3N_4 and BPS-CN. Further, the flat band potential (E_{fb}) of g-C_3N_4 and BPS-CN were also measured by Mott-Schottky (MS) plots under the frequency of 500 Hz, 750 Hz, and 1000 Hz, and the value of E_{fb} can be approximated as the x-intercept at the intersection of three lines in the MS plot [59]. As presented in Fig. 5, the E_{fb} of g-C_3N_4 and BPS-CN are obtained to be −0.81 V and −0.45 V versus an Ag/AgCl electrode (SCE), respectively. Since the positive slope curves determine the samples are n-type semiconductor, the CB potentials are generally considered to be more negative by 0.2 V than E_{fb} ($E_{CB} \approx E_{fb} - 0.2$) [16]. Therefore, the E_{CB} of g-C_3N_4 and BPS-CN are −1.01 eV and −0.65 eV, which are consistent with the above calculated results.

The Photoluminescence (PL) spectrum is an effective way to conduct the migration, transfer and recombination of photogenerated electron-hole pairs in photocatalysts. Generally, stronger PL intensity represents higher recombination efficiency of the photogenerated electron-hole pairs. The catalysts were examined at the excitation wavelength of 350 nm. As displayed in Fig. 6a, g-C_3N_4 displays the highest PL emission peak at about 463 nm, while BPS-CN possesses a much weaker peak intensity at 478 nm. This phenomenon indicates that BPS is successfully doped into the g-C_3N_4 framework and the separation efficiency of photogenerated electron-hole pairs is promoted. Furthermore, BNQDs/BPS-CN shows the weakest peak intensity among all the

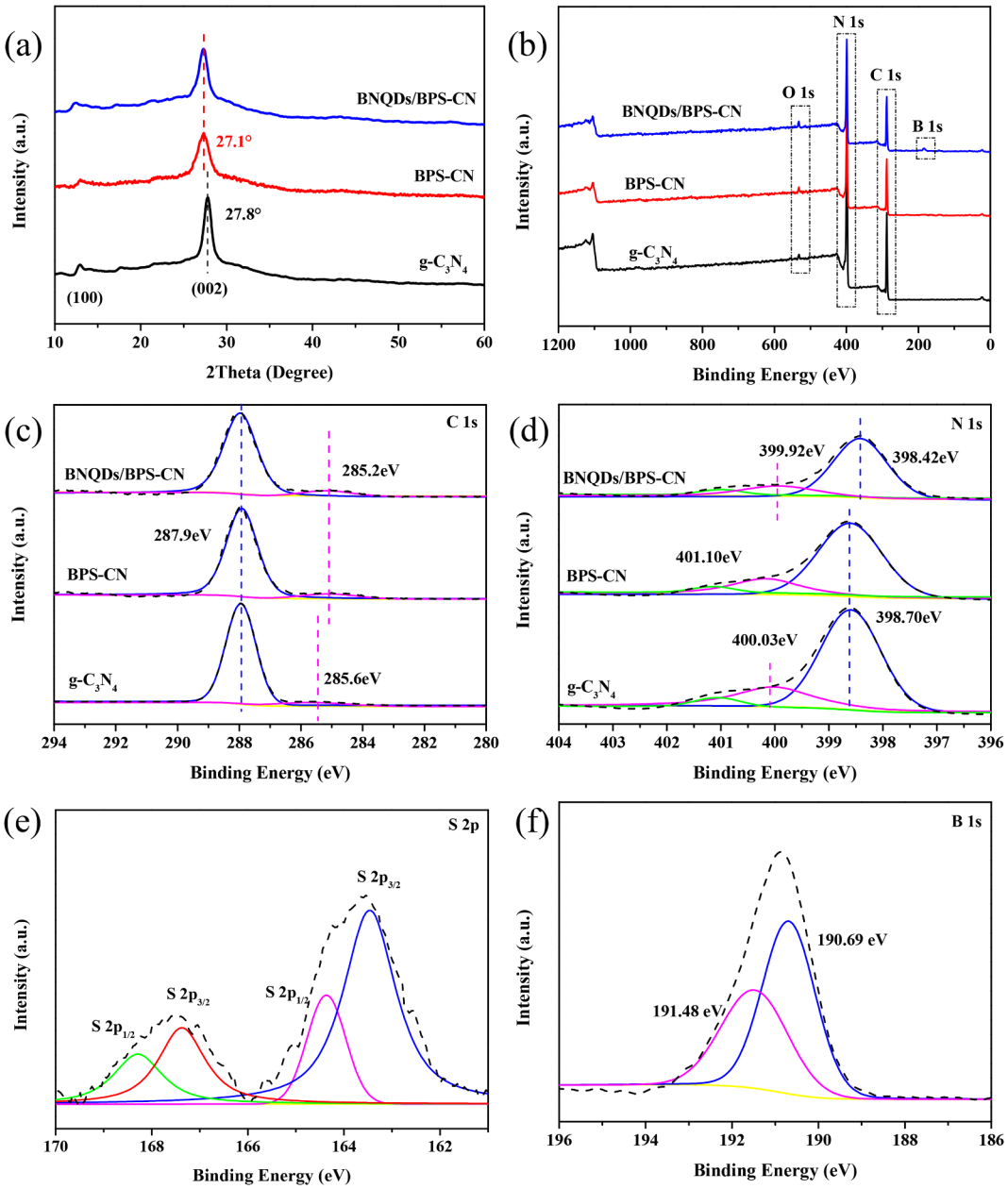

Fig. 2. (a) XRD patterns of different samples; XPS spectra of g-C_3N_4, BPS-CN and BNQDs/BPS-CN samples: (b) total survey, (c) C 1s, (d) N 1s, (e) S 2p, (f) B 1s.

samples, indicating the recombination of photogenerated charge carriers is efficiently inhibited. This may due to the electronegativity of BNQDs attract the photogenerated holes in BPS-CN.

To further explore the separation and transfer process of photogenerated charge carriers, time-resolved photoluminescence (TRPL) decay spectra were used. These decay curves (Fig. 6b) can be well fitted by a biexponential decay function:

$$R(t) = A_1 \exp\left(-\frac{t}{\tau_1}\right) + A_2 \exp\left(-\frac{t}{\tau_2}\right) \quad (2)$$

where τ_1 and τ_2 are the fluorescent lifetime, A_1 and A_2 are the corresponding PL amplitudes. The fitting parameters of g-C_3N_4, BPS-CN, and BNQDs/BPS-CN are listed in Table S2. The average charge carrier lifetime (τ_{ave}) of the samples are calculated by the following equation:

$$\tau_{ave} = \sum A_i \tau_i^2 / \sum A_i \tau_i \quad (3)$$

The average charge carrier lifetime of g-C_3N_4, BPS-CN, and BNQDs/BPS-CN are then calculated to be 5.08, 3.35 and 1.26 ns, respectively, indicating that the charge separation and transfer in g-C_3N_4 is effectively improved after introducing BPS and BNQDs. This observed shortening of average lifetime reveals the emergence of an additional nonradiative quenching pathway in BNQDs/BPS-CN composite due to the presence of doped BNQDs as a hole trap. The results are well consistent with those of PL measurement.

The transient photocurrent measurement was also employed to investigate the separation properties of photogenerated charge carriers in photocatalysis. The transient photocurrent response curves of the samples change orderly with the visible light irradiation on or off. The higher photocurrent density indicates higher separation efficiency of the photogenerated charge carriers. From Fig. 6c, the photocurrent density of BPS-CN is about 2 times higher than g-C_3N_4 nanosheets. As expected, BNQDs/BPS-CN composite exhibits the highest photocurrent density, inferring that the introduction of BNQDs can also accelerate the charges transportation.

Electrochemical impedance spectra (EIS) were used to further

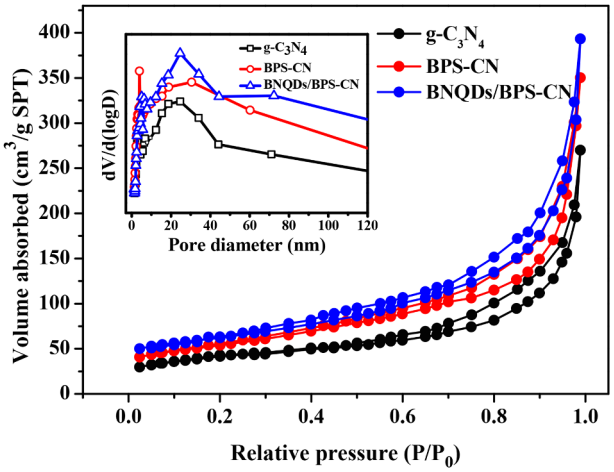

Fig. 3. N_2-sorption isotherms and the pore size distribution (insert).

investigate the enhanced photogenerated charge transfer behavior. Generally, a smaller semicircle diameter in the Nyquist plot reflects a higher efficiency of interfacial charge transfer [26]. As shown in Fig. 6d, the semicircle diameter of the catalysts is arranged as follows: g-C_3N_4 > BPS-CN > BNQDs/BPS-CN, which reveals that BNQDs/BPS-CN possesses the highest charge transfer efficiency.

3.2. Photocatalytic activity and photocatalytic stablity

The photocatalytic activities of all as-prepared samples were evaluated by the degradation experiments of SMZ under the visible light. SMZ is a kind of synthetic sulfonamides that is hard to degrade under natural conditions [9]. Before illumination, the suspension was adequately stirred for 30 min in the dark to achieve the equilibrium of dissolution and adsorption. As shown in Fig. 7a, the adsorption rates of all materials towards SMZ are low (less than 4% after 30 min). When exposed to visible light for 60 min, SMZ is hardly removed in the absence of photocatalyst, verifying its recalcitrance to visible light photolysis. Only 24% SMZ is removed with pure g-C_3N_4 nanosheets as the photocatalyst after 60 min of irradiation. When BPS doped g-C_3N_4 nanosheets (BPS-CN-30) is used as the photocatalyst, the removal of SMZ is increased to 40% under the same reaction conditions (Fig. S6). Strikingly, when using 1 mL of BNQDs alcohol solution (1 mg L^{-1}) decorated BPS-CN as a photocatalyst, more than 97% of SMZ is removed. Meanwhile, when the volume of BNQDs alcohol solution is increased from 1 mL to 4 mL, the removal efficiency of SMZ has increased accordingly to 100%.

The mineralization rates of SMZ with different samples were also studied. As displayed in Fig. 7b, only 10.6% TOC is removed with pure g-C_3N_4 as the photocatalyst after 60 min of irradiation. However, the TOC removal is increased to 40.2% in the presence of BPS-CN-30 after 1 h of irradiation. When BNQDs/BPS-CN-4 is used as the photocatalyst, the TOC removal is further increased to 67.3%. According to the above results, we can indicate that BNQDs/BPS-CN-4 composite is an efficient photocatalyst for SMZ degradation.

The degradation kinetics of SMZ was studied by fitting the reaction kinetics curve, which was simulated by the following equation:

$$-\ln(C_t/C_0) = kt \quad (4)$$

where C_t and C_0 are the SMZ concentration after t minutes of illumination and the initial concentration of SMZ, respectively; k is the apparent pseudo-first-order rate.

As displayed in Fig. 7c, the k for SMZ degradation with BNQDs/BPS-CN-4 as the photocatalyst is 0.0247 min^{-1}, which is 7.06, 13.72 times higher than that of with BPS-CN-30 (0.0035 min^{-1}) and g-C_3N_4 (0.0018 min^{-1}), respectively. The results demonstrate that the BPS doping and the introduction of BNQDs can significantly enhance the photocatalytic performance. In addition, the HPLC chromatogram of SMZ degradation is shown in Fig. S8. It can be seen the retention time of SMZ is about 4.10 min. The intensity of the characteristic peak is decreased with the increase of light duration, and the peak completely disappears after 60 min of irradiation. At the same time, a new peak with a retention time of 4.2 min appears, implying that SMZ is transformed into some new substances.

Besides, investigations were implemented to evaluate the influences of initial pH and coexisting inorganic salts on the degradation of SMZ. As shown in Fig. 7d, the photodegradation of SMZ can efficiently occur at a wild pH range from 5 to 11, with the removal efficiency of above 96% after 60 min of illumination. However, when the initial pH is 3, the removal of SMZ is only 63% at the same time. This may be because SMZ exists in a molecular form at pH 3, which is more difficult to be degraded than SMZ^- ions [60]. Fig. 7e shows the influence of inorganic anions (5 mmol/L) on SMZ degradation. The presence of SO_4^{2-}, $PO_4^{3-}$and Cl^- slightly inhibits the degradation of SMZ, which may be because these anions compete with SMZ for the free radicals produced in the reaction. On the contrary, CO_3^{2-} and NO_3^- promote the degradation of SMZ. Although CO_3^{2-} consumes the free radicals produced in the reaction, it reacts more readily with the aniline moiety of SMZ molecule and thus makes up for the consumption of free radicals [61,62]. Besides, CO_3^{2-} as a pH buffer can maintain the solution at a

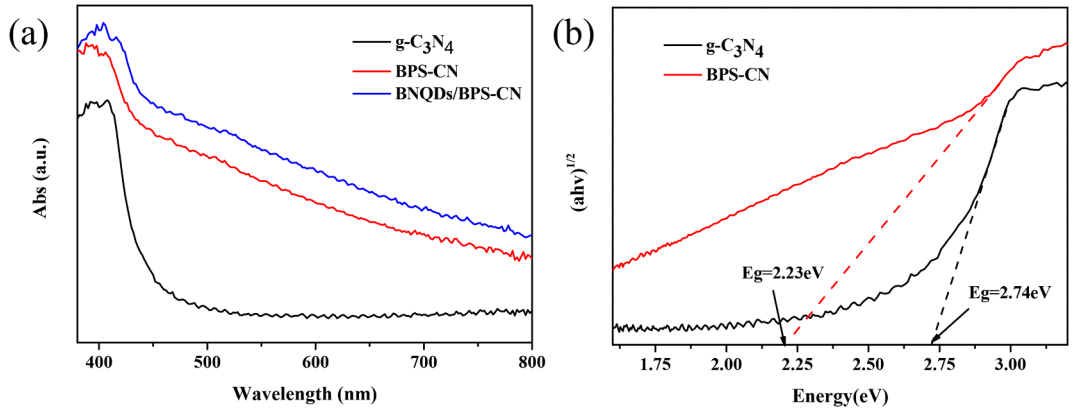

Fig. 4. (a) UV–vis diffuse reflectance spectra of g-C_3N_4, BPS-CN and BNQDs/BPS-CN, (b) Tauc's plots of $(\alpha hv)^{1/2}$ vs. photon energy (hv).

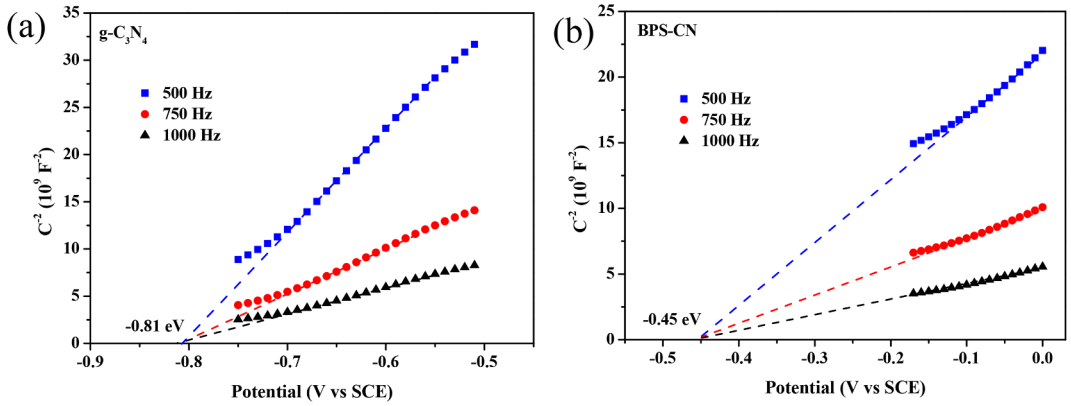

Fig. 5. The Mott–Schottky plots of (a) g-C_3N_4 and (b) BPS-CN samples.

relatively higher pH environment which is beneficial to the reaction [1,63]. Under the light irradiation, NO_3^- can absorb photons and react with water to produce active substances such as nitroso and ·OH, which can promote the photodegradation of SMZ [64,65].

Subsequently, LC-MS was employed to confirm the possible degradation intermediates in the degradation process of SMZ over BNQDs/BPS-CN-4 composite. The corresponding MS spectra and possible intermediates are shown in Fig. S9. High signal intensity can be found at *m/z* 279, corresponding to SMZ (Fig. S9a). Based on the confirmed intermediate products and pertinent literatures, three possible photocatalytic degradation pathways of SMZ are speculated and shown in Fig. 8. Pathway 1 is mainly the hydroxylation process. The aniline moiety of SMZ is oxidized by ·*OH* to form P1 (*m/z* 295) and then the S-N bond is induced to breakage to generate sulfanilic acid labeled as P2 (*m/z* 189), finally, P2 is oxidized to P3 (*m/z* 110) via hydroxylation reactions [66]. Pathway 2 mainly includes the detachment of the sulfonyl group and the cleavage of the C-N bond. SMZ lost the sulfonyl group and change to P4 (*m/z* 215) [14], and then the C-N bond in P4 is oxidized and cleaved to form P5 (*m/z* 109) and P6 (*m/z* 124). Pathway 3 mainly contains the cleavage and of the S-N bond in

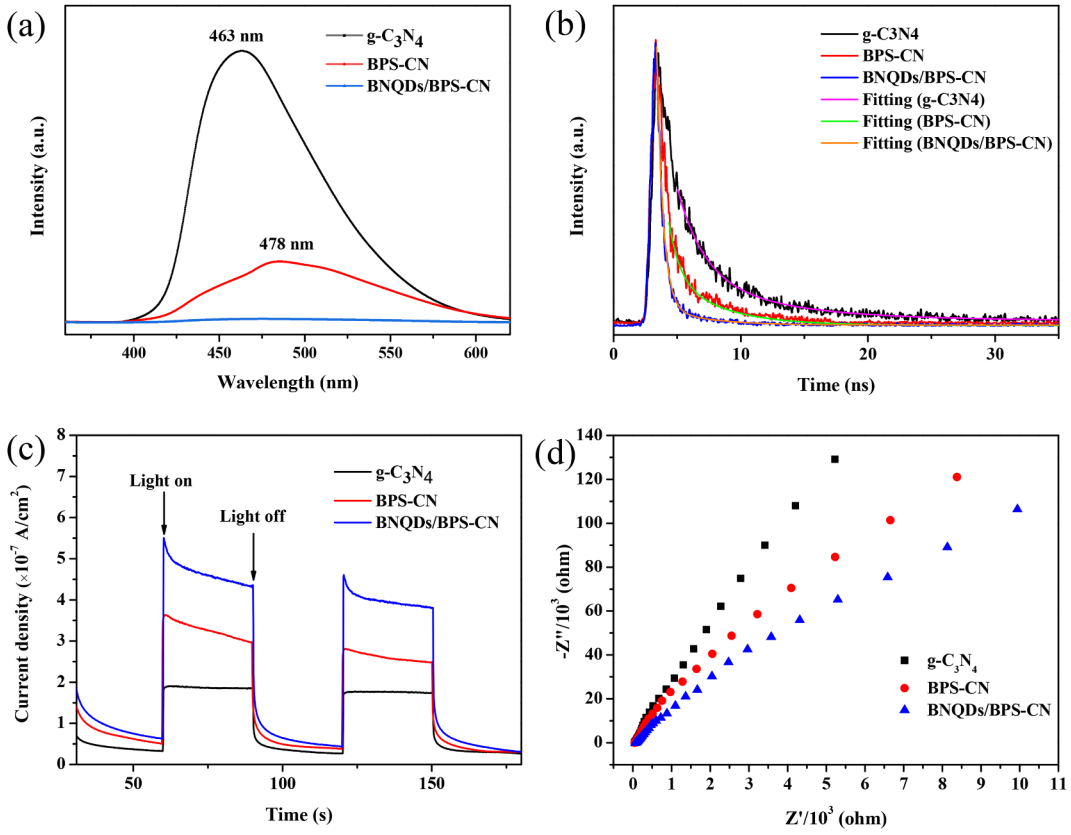

Fig. 6. (a) The PL spectra, (b) time-resolved photoluminescence decay spectra, (c) Transient photocurrent response curves, (d) EIS Nyquist plots of g-C_3N_4, BPS-CN and BNQDs/BPS-CN.

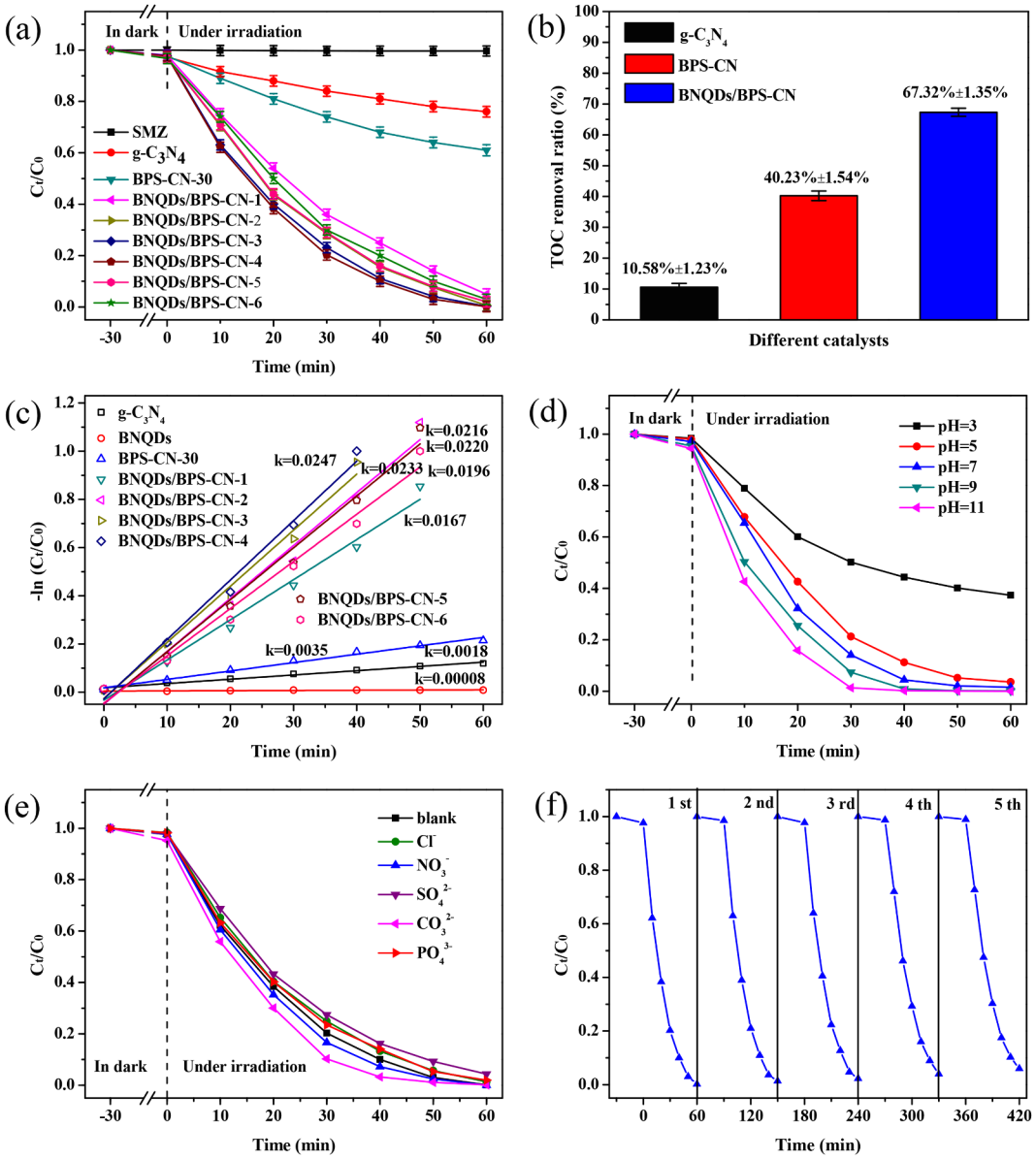

Fig. 7. (a) Photodegradation curves, (b) TOC removal of SMZ and (c) reaction kinetic curves under visible light irradiation (λ > 420 nm) for different samples; (d) photodegradation curves of SMZ at different pH condition and (e) with different anions (f) cycling test for the photocatalytic degradation for BNQDs/BPS-CN.

SMZ. The S–N bond in SMZ cleaves to form P6 (*m/z* 124) and P7 (*m/z* 174), and then P7 is changed to P5 via oxidation reaction. These results indicate that the detectable degradation products are mainly bisphenol A, p-aminophenol, and other inorganics, which are easier to biodegrade than SMZ.

The reusability and stability of the obtained BNQDs/BPS-CN composite was also investigated. Fig. 7f shows the removal of SMZ can still reach more than 95% even after five cycles, which implies the good stability of the BNQDs/BPS-CN composite. In addition, the XRD patterns of fresh and used BNQDs/BPS-CN are almost identical (Fig. S10). These results further demonstrate that the as-prepared BNQDs/BPS-CN catalyst is sufficiently stable during the photodegradation of SMZ.

3.3. Possible photocatalytic mechanism

To illustrate the photocatalytic degradation mechanism of SMZ with BNQDs/BPS-CN photocatalyst, the main active species trapping experiments were executed. The isopropanol (IPA), benzoquinone (BQ), and ethylenediamine tetra acetic acid disodium salt (EDTA-2Na) are used as the hydroxyl radical (·OH) scavenger, superoxide radical (·O_2^-) scavenger and hole (h^+) scavenger, respectively [67]. As exhibited in Fig. 9a, the removal of SMZ is significantly reduced from 100% to 28.1% with the addition of BQ and to 11.8% in the presence of EDTA-2Na, implying that ·O_2^- and h^+ play the major roles in the photodegradation of SMZ. Whereas, there is only a slight decrease in SMZ degradation in the existence of IPA, indicating that ·OH only has a slight influence on SMZ degradation. According to these above results, it can be inferred that h^+ and ·O_2^- are the main reactive species in the degradation process of SMZ with BNQDs/BPS-CN.

To further verify the generation of the related active species in the photocatalytic system, the electron spin resonance (ESR) spin-trap technique with the signals of ·O_2^- and ·OH radicals was performed. And the radical generation experiments of g-C_3N_4, BPS-CN, BNQDs/BPS-CN were conducted in darkness, 5 min and 10 min irradiation conditions. As shown in Fig. 9b and c, there is no obvious signal in the dark, however, when exposed to visible light, the characteristic signals of DMPO-·O_2^- can be found and the signal intensity increases with prolonging the irradiation time, suggesting that ·O_2^- is formed in the

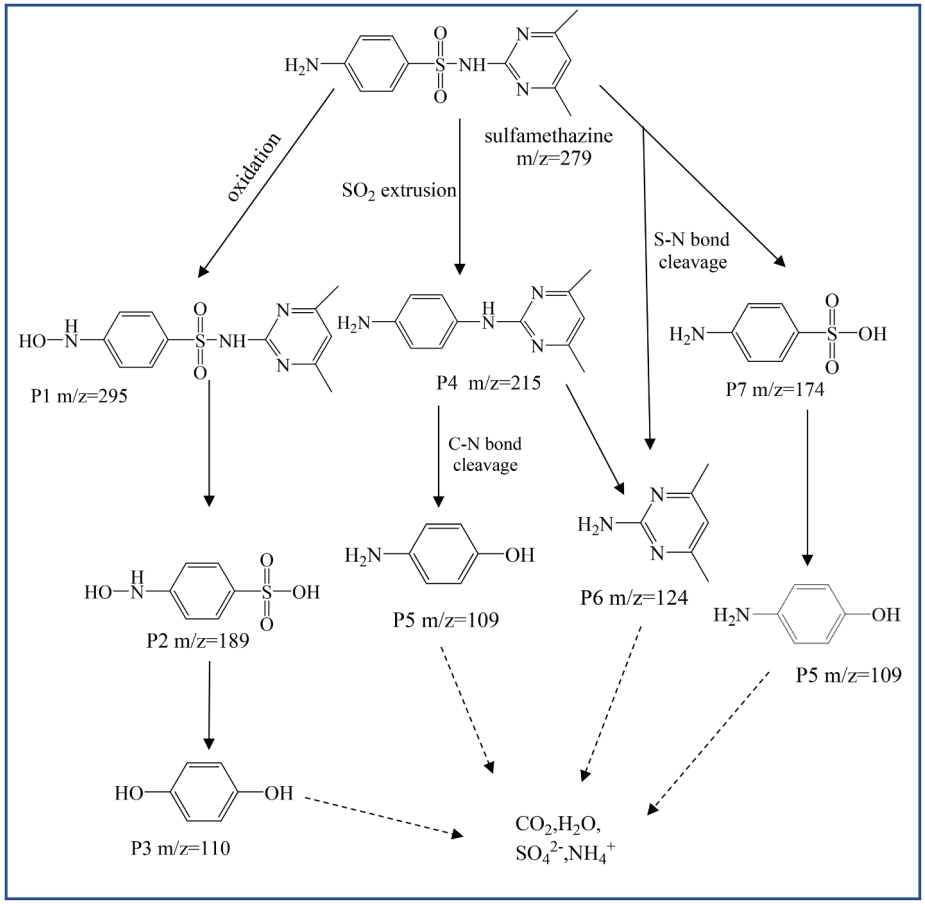

Fig. 8. A possible photocatalytic degradation pathway of SMZ.

photocatalytic system. Meanwhile, it is obvious that the DMPO-$\cdot O_2^-$ signal in the BNQDs/BPS-CN system is stronger than that in the g-C_3N_4 or BPS-CN system. This may be due to the excellent photo-induced carrier separation ability of BNQDs/BPS-CN, leading to the generation of more $\cdot O_2^-$. Moreover, more photogenerated electrons in the BNQDs/BPS-CN system make the DMPO-$\cdot$OH signal also stronger than that in the g-C_3N_4 or BPS-CN system.

Base on the above experimental results and analysis, a tentative photocatalytic degradation mechanism SMZ over BNQDS/BPS-CN was put forward. As illustrated in Fig. 10, the E_{VB} and E_{CB} of BPS-CN are calculated to 1.57 eV and −0.65 eV, respectively. When exposed to visible light, BPS-CN nanosheets can absorb more photons due to the narrower band gap and thus more electrons at valence band are easily excited and transferred to the conduction band. Meanwhile, BNQDs on the surface of BPS-CN can efficiently attract and transfer the photo-excited holes, effectively inhibiting the recombination of electron-hole pairs and improving the photogenerated charge carriers separation. (Eq. (5)). Moreover, the doping of BPS and the introduction of BNQDs increase the surface area of g-C_3N_4, which offers more reaction sites and further improves the photocatalytic activity of g-C_3N_4. During the photocatalytic degradation process, photogenerated electrons react with molecules adsorbed on the catalyst surface to form $\cdot O_2^-$, owing to the CB potentials of BPS-CN (−0.65 eV) is more negative than the $O_2/\cdot O_2^-$ potential (−0.33 eV vs. NHE) (Eq. (6)). Then the electrons and $\cdot O_2^-$ reacts with H^+ to generate H_2O_2 (Eq. (7)) and further produces $\cdot$OH (Eq. (8)). Therefore, the reactive species such as h^+,$\cdot O_2^-$ and $\cdot$OH on the surface of BNQDs/BPS-CN collectively lead to the degradation of SMZ (Eq. (9)).

$$BNQDs/BPS - CN + hv \rightarrow h^+ + e^- \quad (5)$$

$$e^- + O_2 \rightarrow \cdot O_2^- \quad (6)$$

$$\cdot O_2^- + 2H^+ + e^- \rightarrow H_2O_2 \quad (7)$$

$$H_2O_2 + e^- \rightarrow OH^- + \cdot OH \quad (8)$$

$$(\cdot O_2^-,\ h+\ ,\cdot OH) + SMZ \rightarrow product \quad (9)$$

4. Conclusions

In summary, metal-free BNQDs/BPS-CN heterojunction photocatalysts were successfully synthesized by a convenient approach. The BNQDs/BPS-CN composite exhibits excellent photocatalytic activities and photostability for SMZ degradation under visible light irradiation. The removal of SMZ reaches 100% after 60 min of irradiation, and the rate constant is 13.7 times higher than pure g-C_3N_4. PL, TRPL and photoelectrochemical tests illustrate a remarkable enhancement in the separation and transfer of photogenerated charge carriers of BNQDs/BPS-CN composite. The results of active species trapping experiments and ESR analysis identify that the photogenerated holes and superoxide radicals play major roles in the photocatalytic degradation of SMZ. This study develops a promising non-metal photocatalyst for the removal of organic pollutants under visible light.

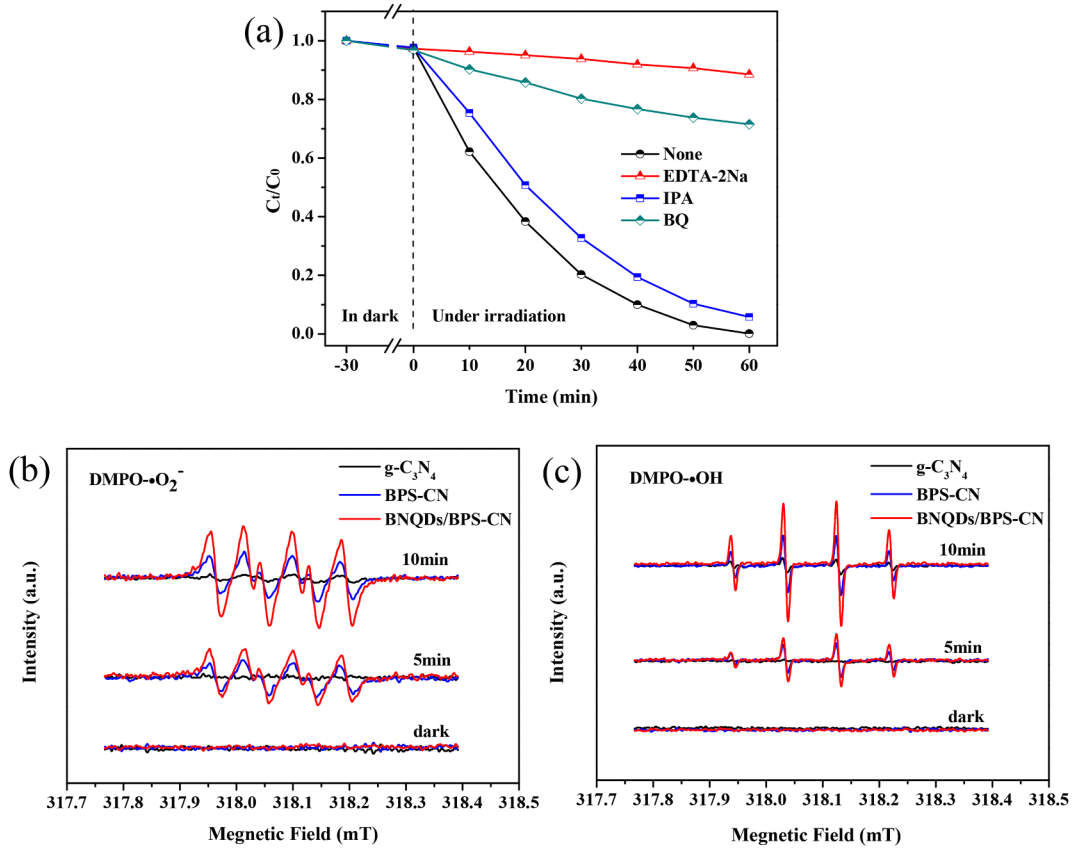

Fig. 9. (a) Photodegradation curves of SMZ over BNQDs/BPS-CN with different quenchers; ESR spectra of (b) DMPO-·O_2^- adduct and (c) DMPO-·OH adduct for different samples under visible light irradiation (λ > 420 nm).

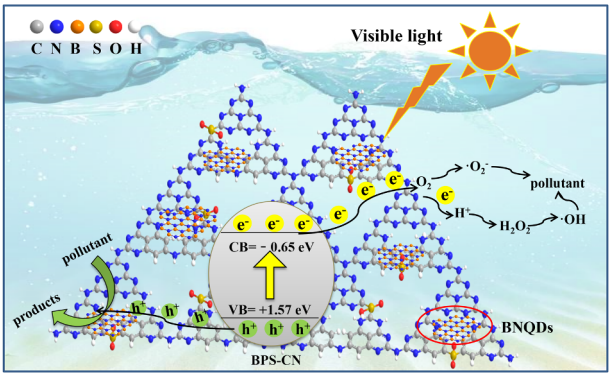

Fig. 10. Schematic illustration of photocatalytic mechanism for BNQDs/BPS-CN composite under visible light irradiation.

Declaration of Competing Interest

The authors declare that they have no known competing financial interests or personal relationships that could have appeared to influence the work reported in this paper.

Acknowledgements

Support from the National Natural Science Foundation of China (Grant No.: 51978178 and 51521006), the Department of Science and Technology of Hunan Province of China (Contract No.: 2018JJ2048, 2017JJ2029 and 2017SK2362), the International S&T Cooperation Program of China (Contract No.: 2015DFG92750), the Department of Science and Technology of Guangdong Province of China (Contract No.: 2019A1515012044), and Maoming Municipal Bureau of Science and Technology of Guangdong Province of China (Contract No.: 2018S0011) is highly appreciated.

Appendix A. Supplementary data

Supplementary data to this article can be found online at https://doi.org/10.1016/j.cej.2020.126661.

References

[1] H. Jiang, C. Zhu, Y. Yuan, C. Yue, C. Ling, F. Liu, A. Li, Enhanced activation of peroxymonosulfate with metal-substituted hollow $MxCo_3$-xS_4 polyhedrons for superfast degradation of sulfamethazine, Chem. Eng. J. 384 (2020) 123302.
[2] H. Hu, Q. Zhou, X. Li, W. Lou, C. Du, Q. Teng, D. Zhang, H. Liu, Y. Zhong, C. Yang, Phytoremediation of anaerobically digested swine wastewater contaminated by oxytetracycline via Lemna aequinoctialis: Nutrient removal, growth characteristics and degradation pathways, Bioresour. Technol. 291 (2019) 121853.
[3] Q. Zhou, X. Li, S. Wu, Y. Zhong, C. Yang, Enhanced strategies for antibiotic removal from swine wastewater in anaerobic digestion, Trends Biotechnol. (2020), https://doi.org/10.1016/j.tibtech.2020.07.002.
[4] H. Zhang, Z. Wang, R. Li, J. Guo, Y. Li, J. Zhu, X. Xie, TiO_2 supported on reed straw biochar as an adsorptive and photocatalytic composite for the efficient degradation of sulfamethoxazole in aqueous matrices, Chemosphere 185 (2017) 351–360.
[5] K. Kümmerer, Antibiotics in the aquatic environment– A review– Part I, Chemosphere 75 (2009) 417–434.
[6] Q. Zhou, X. Li, Y. Lin, C. Yang, W. Tang, S. Wu, D. Li, W. Lou, Effects of copper ions on removal of nutrients from swine wastewater and on release of dissolved organic matter in duckweed systems, Water Res. 158 (2019) 171–181.
[7] J.A. Gao, J.A. Pedersen, Adsorption of sulfonamide antimicrobial agents to clay minerals, Environ. Sci. Technol. 39 (2005) 9509–9516.
[8] Q. Luo, Q. Zhou, Y. Lin, S. Wu, H. Liu, C. Du, Y. Zhong, C. Yang, Fast and deep oxidative desulfurization of dibenzothiophene with catalysts of MoO_3-TiO_2@MCM-22 featuring adjustable Lewis and Bronsted acid sites, Catal. Sci. Technol. 9 (2019) 6166–6179.
[9] N. Barhoumi, N. Oturan, H. Olvera-Vargas, E. Brillas, A. Gadri, S. Ammar, M.A. Oturan, Pyrite as a sustainable catalyst in electro-Fenton process for improving oxidation of sulfamethazine: Kinetics, mechanism and toxicity assessment, Water

Res. 94 (2016) 52–61.
[10] S. Wu, H. Liu, Y. Lin, C. Yang, W. Lou, J. Sun, C. Du, D. Zhang, L. Nie, K. Yin, Y. Zhong, Insights into mechanisms of UV/ferrate oxidation for degradation of phenolic pollutants: Role of superoxide radicals, Chemosphere 244 (2020) 125490-125490.
[11] S. Wu, H. Liu, C. Yang, X. Li, Y. Lin, K. Yin, J. Sun, Q. Teng, C. Du, Y. Zhong, High-performance porous carbon catalysts doped by iron and nitrogen for degradation of bisphenol F via peroxymonosulfate activation, Chem. Eng. J. 392 (2020) 123683.
[12] H.P. Feng, J.F. Yu, L. Tang, G.M. Zeng, W.W. Tang, J.J. Wang, T. Luo, B. Peng, B. Song, L.L. Wang, C. Liang, Tuning electron density endows Fe_1-xCoxP with exceptional capability of electrooxidation of organic pollutants, Environ. Sci. Technol. 53 (2019) 13878–13887.
[13] Y. Lin, C.P. Yang, S.H. Wu, X. Li, Y.J. Chen, W.L. Yang, Construction of built-in electric field within silver phosphate photocatalyst for enhanced removal of recalcitrant organic pollutants, Adv. Funct. Mater. (2020) 2002918, , https://doi.org/10.1002/adfm.202002918.
[14] S. Cao, Z. Jiao, H. Chen, F. Jiang, X. Wang, Carboxylic acid-functionalized cadmium sulfide/graphitic carbon nitride composite photocatalyst with well-combined interface for sulfamethazine degradation, J. Photoch. Photobio. A 364 (2018) 22–31.
[15] D. Shindell, C.J. Smith, Climate and air-quality benefits of a realistic phase-out of fossil fuels, Nature 573 (2019) 408–411.
[16] Y. Lin, S. Wu, X. Li, X. Wu, C. Yang, G. Zeng, Y. Peng, Q. Zhou, L. Lu, Microstructure and performance of Z-scheme photocatalyst of silver phosphate modified by MWCNTs and Cr-doped $SrTiO_3$ for malachite green degradation, Appl. Catal. B Environ. 227 (2018) 557–570.
[17] Y. Yang, C. Zhang, D. Huang, G. Zeng, J. Huang, C. Lai, C. Zhou, W. Wang, H. Guo, W. Xue, R. Deng, M. Cheng, W. Xiong, Boron nitride quantum dots decorated ultrathin porous g-C_3N_4: Intensified exciton dissociation and charge transfer for promoting visible-light-driven molecular oxygen activation, Appl. Catal. B Environ. 245 (2019) 87–99.
[18] C. Zhou, C. Lai, D. Huang, G. Zeng, C. Zhang, M. Cheng, L. Hu, J. Wan, W. Xiong, M. Wen, X. Wen, L. Qin, Highly porous carbon nitride by supramolecular preassembly of monomers for photocatalytic removal of sulfamethazine under visible light driven, Appl. Catal. B Environ. 220 (2018) 202–210.
[19] S. Thaweesak, M. Lyu, P. Peerakiatkhajohn, T. Butburee, B. Luo, H. Chen, L. Wang, Two-dimensional g-C_3N_4/$Ca_2Nb_2TaO_{10}$ nanosheet composites for efficient visible light photocatalytic hydrogen evolution, Appl. Catal. B Environ. 202 (2017) 184–190.
[20] Y. Shiraishi, S. Kanazawa, Y. Sugano, D. Tsukamoto, H. Sakamoto, S. Ichikawa, T. Hirai, Highly selective production of hydrogen peroxide on graphitic carbon nitride (g-C_3N_4) photocatalyst activated by visible light, ACS Catal. 4 (2014) 774–780.
[21] Y. Sheng, Z. Wei, H. Miao, W. Yao, H. Li, Y. Zhu, Enhanced organic pollutant photodegradation via adsorption/photocatalysis synergy using a 3D g-C_3N_4/TiO_2 free-separation photocatalyst, Chem. Eng. J. 370 (2019) 287–294.
[22] F. Nekouei, S. Nekouei, M. Pouzesh, Y. Liu, Porous-CdS/Cu_2O/graphitic-C_3N_4 dual p-n junctions as highly efficient photo/catalysts for degrading ciprofloxacin and generating hydrogen using solar energy, Chem. Eng. J. 385 (2020) 123710.
[23] Y. Shiraishi, Y. Kofuji, H. Sakamoto, S. Tanaka, S. Ichikawa, T. Hirai, Effects of surface defects on photocatalytic H_2O_2 production by mesoporous graphitic carbon nitride under visible light irradiation, ACS Catal. 5 (2015) 3058–3066.
[24] G.-H. Moon, M. Fujitsuka, S. Kim, T. Majima, X. Wang, W. Choi, Eco-friendly photochemical production of H_2O_2 through O_2 reduction over carbon nitride frameworks incorporated with multiple heteroelements, ACS Catal. 7 (2017) 2886–2895.
[25] Q. Han, B. Wang, Y. Zhao, C. Hu, L. Qu, A graphitic-C_3N_4 "seaweed" architecture for enhanced hydrogen evolution, Angew. Chem. Int. Edit 54 (2015) 11433–11437.
[26] J. Bai, C. Yin, H. Xu, G. Chen, Z. Ni, Z. Wang, Y. Li, S. Kang, Z. Zheng, X. Li, Facile urea-assisted precursor pre-treatment to fabricate porous g-C_3N_4 nanosheets for remarkably enhanced visible-light-driven hydrogen evolution, J. Colloid Interf. Sci. 532 (2018) 280–286.
[27] M. Sumathi, A. Prakasam, P.M. Anbarasan, Fabrication of ultrathin nanosheets of graphitic carbon nitride heterojunction with spherical shaped Bi_2O_3 nanoparticles for high performance visible light photocatalyst, J. Clust. Sci. 31 (2020) 277–286.
[28] L. Jiang, X. Yuan, G. Zeng, J. Liang, Z. Wu, H. Yu, D. Mo, H. Wang, Z. Xiao, C. Zhou, Nitrogen self-doped g-C_3N_4 nanosheets with tunable band structures for enhanced photocatalytic tetracycline degradation, J. Colloid Interf. Sci. 536 (2019) 17–29.
[29] L. Jiang, X. Yuan, G. Zeng, X. Chen, Z. Wu, J. Liang, J. Zhang, H. Wang, H. Wang, Phosphorus- and sulfur-codoped g-C_3N_4: facile preparation, mechanism insight, and application as efficient photocatalyst for tetracycline and methyl orange degradation under visible light irradiation, ACS Sustain. Chem. Eng. 5 (2017) 5831–5841.
[30] A. Tripathi, S. Narayanan, Potassium doped graphitic carbon nitride with extended optical absorbance for solar light driven photocatalysis, Appl. Surf. Sci. 479 (2019) 1–11.
[31] K. Li, M. Sun, W.-D. Zhang, Polycyclic aromatic compounds-modified graphitic carbon nitride for efficient visible-light-driven hydrogen evolution, Carbon 134 (2018) 134–144.
[32] N. Karjule, J. Barrio, J. Tzadikov, M. Shalom, Electronic structure engineering of carbon nitride materials by using polycyclic aromatic hydrocarbons, Chem. Eur. J. 26 (2020) 6622–6628.
[33] J. Tan, B. Peng, L. Tang, C. Feng, J. Wang, J. Yu, X. Ouyang, X. Zhu, Enhanced photoelectric conversion efficiency: a novel h-BN based self-powered photoelectrochemical aptasensor for ultrasensitive detection of diazinon, Biosens. Bioelectron. 142 (2019) 111546.
[34] Z.G. Mou, C. Lu, K. Yu, H. Wu, H. Zhang, J.H. Sun, M.S. Zhu, M.C. Goh, Chemical interaction in nitrogen-doped graphene quantum dots/graphitic carbon nitride heterostructures with enhanced photocatalytic H_2 evolution, Energy Technol. Ger. 7 (2019) 1800589.
[35] J. Lv, K. Dai, J. Zhang, Q. Liu, C. Liang, G. Zhu, Facile constructing novel 2D porous g-C_3N_4/BiOBr hybrid with enhanced visible-light-driven photocatalytic activity, Sep. Purif. Technol. 178 (2017) 6–17.
[36] A. Pakdel, Y. Bando, D. Golberg, Nano boron nitride flatland, Chem. Soc. Rev. 43 (2014) 934–959.
[37] K. Watanabe, T. Taniguchi, H. Kanda, Direct-bandgap properties and evidence for ultraviolet lasing of hexagonal boron nitride single crystal, Nat. Mater. 3 (2004) 404–409.
[38] D. Golberg, Y. Bando, Y. Huang, T. Terao, M. Mitome, C. Tang, C. Zhi, Boron nitride nanotubes and nanosheets, ACS Nano 4 (2010) 2979–2993.
[39] S. Ding, D. Mao, S. Yang, F. Wang, L. Meng, M. Han, H. He, C. Sun, B. Xu, Graphene-analogue h-BN coupled Bi-rich Bi_4O_5Br 2 layered microspheres for enhanced visible-light photocatalytic activity and mechanism insight, Appl. Catal. B: Environ. 210 (2017) 386–399.
[40] J. Di, J. Xia, M. Ji, B. Wang, S. Yin, Q. Zhang, Z. Chen, H. Li, Advanced photocatalytic performance of graphene-like BN modified BiOBr flower-like materials for the removal of pollutants and mechanism insight, Appl. Catal. B Environ. 183 (2016) 254–262.
[41] Y. Jiao, Q. Huang, J. Wang, Z. He, Z. Li, A novel MoS_2 quantum dots (QDs) decorated Z-scheme g-C_3N_4 nanosheet/N-doped carbon dots heterostructure photocatalyst for photocatalytic hydrogen evolution, Appl. Catal. B Environ. 247 (2019) 124–132.
[42] L.K. Putri, B.-J. Ng, W.-J. Ong, H.W. Lee, W.S. Chang, A.R. Mohamed, S.-P. Chai, Energy level tuning of CdSe colloidal quantum dots in ternary 0D–2D-2D CdSe QD/B-rGO/O-gC_3N_4 as photocatalysts for enhanced hydrogen generation, Appl. Catal. B Environ. 265 (2020) 118592.
[43] H. Li, R.Y. Tay, S.H. Tsang, X. Zhen, E.H. Teo, Controllable synthesis of highly luminescent boron nitride quantum dots, Small 11 (2015) 6491–6499.
[44] M.L. Liu, Y.H. Xu, Y. Wang, X. Chen, X.Q. Ji, F.S. Niu, Z.Q. Song, J.Q. Liu, Boron nitride quantum dots with solvent-regulated blue/green photoluminescence and electrochemiluminescent behavior for versatile applications, Adv. Opt. Mater. 5 (2017).
[45] C. Zhou, C. Lai, C. Zhang, G. Zeng, D. Huang, M. Cheng, L. Hu, W. Xiong, M. Chen, J. Wang, Y. Yang, L. Jiang, Semiconductor/boron nitride composites: Synthesis, properties, and photocatalysis applications, Appl. Catal. B Environ. 238 (2018) 6–18.
[46] J. Liu, Y. Yu, R. Qi, C. Cao, X. Liu, Y. Zheng, W. Song, Enhanced electron separation on in-plane benzene-ring doped g-C_3N_4 nanosheets for visible light photocatalytic hydrogen evolution, Appl. Catal. B Environ. 244 (2019) 459–464.
[47] B. Huo, B. Liu, T. Chen, L. Cui, G. Xu, M. Liu, J. Liu, One-Step synthesis of fluorescent boron nitride quantum dots via a hydrothermal strategy using melamine as nitrogen source for the detection of ferric ions, Langmuir 33 (2017) 10673–10678.
[48] X. Zhu, L. Gao, L. Tang, B. Peng, H. Huang, J. Wang, J. Yu, X. Ouyang, J. Tan, Ultrathin PtNi nanozyme based self-powered photoelectrochemical aptasensor for ultrasensitive chloramphenicol detection, Biosens. Bioelectron. 146 (2019) 111756.
[49] L. Lin, Y. Xu, S. Zhang, I.M. Ross, A.C.M. Ong, D.A. Allwood, Fabrication and luminescence of monolayered boron nitride quantum dots, Small 10 (2014) 60–65.
[50] T. Giannakopoulou, I. Papailias, N. Todorova, N. Boukos, Y. Liu, J. Yu, C. Trapalis, Tailoring the energy band gap and edges' potentials of g-C_3N_4/TiO_2 composite photocatalysts for NOx removal, Chem. Eng. J. 310 (2017) 571–580.
[51] J. Zhang, G. Zhang, X. Chen, S. Lin, L. Mohlmann, G. Dolega, G. Lipner, M. Antonietti, S. Blechert, X. Wang, Co-monomer control of carbon nitride semiconductors to optimize hydrogen evolution with visible light, Angew. Chem. Int. Ed. Engl. 51 (2012) 3183–3187.
[52] Z. He, C. Kim, L. Lin, T.H. Jeon, S. Lin, X. Wang, W. Choi, Formation of heterostructures via direct growth CN on h-BN porous nanosheets for metal-free photocatalysis, Nano Energy 42 (2017) 58–68.
[53] Y.L. Yang, S.C. Wang, Y.L. Jiao, Z.L. Wang, M. Xiao, A.J. Du, Y.L. Li, J.S. Wang, L.Z. Wang, An unusual red carbon nitride to boost the photoelectrochemical performance of wide bandgap photoanodes, Adv. Funct. Mater. 28 (2018) 1805698.
[54] C.Y. Feng, L. Tang, Y.C. Deng, G.M. Zeng, J.J. Wang, Y.N. Liu, Z.M. Chen, J.F. Yu, J.J. Wang, Enhancing optical absorption and charge transfer: synthesis of S-doped h-BN with tunable band structures for metal-free visible-light-driven photocatalysis, Appl. Catal. B: Environ. 256 (2019).
[55] S.B. Yang, L.J. Zhi, K. Tang, X.L. Feng, J. Maier, K. Mullen, Efficient synthesis of heteroatom (N or S)-doped graphene based on ultrathin graphene oxide-porous silica sheets for oxygen reduction reactions, Adv. Funct. Mater. 22 (2012) 3634–3640.
[56] X. Zheng, J. Wu, X. Cao, J. Abbott, C. Jin, H. Wang, P. Strasser, R. Yang, X. Chen, G. Wu, N-, P-, and S-doped graphene-like carbon catalysts derived from onium salts with enhanced oxygen chemisorption for Zn-air battery cathodes, Appl. Catal. B Environ. 241 (2019) 442–451.
[57] L. Li, W. Fang, P. Zhang, J. Bi, Y. He, J. Wang, W. Su, Sulfur-doped covalent triazine-based frameworks for enhanced photocatalytic hydrogen evolution from water under visible light, J. Mater. Chem. A 4 (2016) 12402–12406.
[58] Y. Zhang, J. Shi, Z. Huang, X. Guan, S. Zong, C. Cheng, B. Zheng, L. Guo, Synchronous construction of CoS_2 in-situ loading and S doping for g-C_3N_4: enhanced photocatalytic H_2-evolution activity and mechanism insight, Chem. Eng. J. 401 (2020) 126135.
[59] Y. Lin, H. Liu, C. Yang, X. Wu, C. Du, L. Jiang, Y. Zhong, Gama-graphyne as photogenerated electrons transfer layer enhances photocatalytic performance of silver phosphate, Appl. Catal. B Environ. 264 (2020) 118479.
[60] M.C. Dodd, M.O. Buffle, U. Von Gunten, Oxidation of antibacterial molecules by aqueous ozone: moiety-specific reaction kinetics and application to ozone-based

wastewater treatment, Environ. Sci. Technol. 40 (2006) 1969–1977.
[61] S. Canonica, T. Kohn, M. Mac, F.J. Real, J. Wirz, U. Von Gunten, Photosensitizer method to determine rate constants for the reaction of carbonate radical with organic compounds, Environ. Sci. Technol. 39 (2005) 9182–9188.
[62] L. Hu, P.M. Flanders, P.L. Miller, T.J. Strathmann, Oxidation of sulfamethoxazole and related antimicrobial agents by TiO_2 photocatalysis, Water Res. 41 (2007) 2612–2626.
[63] Y. Fan, Y. Ji, D. Kong, J. Lu, Q. Zhou, Kinetic and mechanistic investigations of the degradation of sulfamethazine in heat-activated persulfate oxidation process, J. Hazard. Mater. 300 (2015) 39–47.
[64] Q.Z. Jia, X.C. Jia, R.M. Li, H. Chen, J.J. Tao, C. Wang, UV-photolysis of sulfamfhnazine: effects of dissoved ions in water and the photodegradation mechanism, Fresen. Environ. Bull. 26 (2017) 3519–3528.
[65] J.L. Peng, G.G. Wang, D.H. Zhang, D.M. Zhang, X.G. Li, Photodegradation of nonylphenol in aqueous solution by simulated solar UV-irradiation: The comprehensive effect of nitrate, ferric ion and bicarbonate, J. Photoch. Photobio. A 326 (2016) 9–15.
[66] J. Wu, B. Wang, L. Blaney, G. Peng, P. Chen, Y. Cui, S. Deng, Y. Wang, J. Huang, G. Yu, Degradation of sulfamethazine by persulfate activated with organo-montmorillonite supported nano-zero valent iron, Chem. Eng. J. 361 (2019) 99–108.
[67] Y. Lin, X. Wu, Y. Han, C. Yang, Y. Ma, C. Du, Q. Teng, H. Liu, Y. Zhong, Spatial separation of photogenerated carriers and enhanced photocatalytic performance on Ag_3PO_4 catalysts via coupling with PPy and MWCNTs, Appl. Catal. B Environ. 258 (2019) 117969.